

Accepted Article

Title: Boosting Photoacoustic Effect via Intramolecular Motions Amplifying Thermal-to-Acoustic Conversion Efficiency for Adaptive Image-Guided Cancer Surgery

Authors: Heqi Gao, Xingchen Duan, Di Jiao, Yi Zeng, Xiaoyan Zheng, Jingtian Zhang, Hanlin Ou, Ji Qi, and Dan Ding

This manuscript has been accepted after peer review and appears as an Accepted Article online prior to editing, proofing, and formal publication of the final Version of Record (VoR). This work is currently citable by using the Digital Object Identifier (DOI) given below. The VoR will be published online in Early View as soon as possible and may be different to this Accepted Article as a result of editing. Readers should obtain the VoR from the journal website shown below when it is published to ensure accuracy of information. The authors are responsible for the content of this Accepted Article.

To be cited as: *Angew. Chem. Int. Ed.* 10.1002/anie.202109048

Link to VoR: <https://doi.org/10.1002/anie.202109048>

RESEARCH ARTICLE

Boosting Photoacoustic Effect via Intramolecular Motions Amplifying Thermal-to-Acoustic Conversion Efficiency for Adaptive Image-Guided Cancer Surgery

Heqi Gao,^{+[a]} Xingchen Duan,^{+[a]} Di Jiao,^[a] Yi Zeng,^[b] Xiaoyan Zheng,^{*[b]} Jingtian Zhang,^[a] Hanlin Ou,^[a] Ji Qi,^{*[a]} and Dan Ding^{*[a]}

[a] Dr. H. Gao, X. Duan, D. Jiao, J. Zhang, Dr. H. Ou, Prof. J. Qi, Prof. D. Ding
State Key Laboratory of Medicinal Chemical Biology, Frontiers Science Center for Cell Responses, Key Laboratory of Bioactive Materials, Ministry of Education, and College of Life Sciences, Nankai University, Tianjin 300071, China
E-mail: qiji@nankai.edu.cn, dingd@nankai.edu.cn.

[b] Y. Zeng, Prof. X. Zheng
Beijing Key Laboratory of Photoelectronic/Electrophotonic Conversion Materials, Key Laboratory of Cluster Science of Ministry of Education, School of Chemistry and Chemical Engineering, Beijing Institute of Technology, Beijing 100081, China
E-mail: xiaoyanzheng@bit.edu.cn.

[*] These authors contributed equally to this work

Supporting information for this article is given via a link at the end of the document.

Abstract: Photoacoustic (PA) imaging emerges as a promising technique for biomedical applications. The development of new strategies to boost PA conversion without depressing other properties (e.g., fluorescence) is highly desirable for multifunctional imaging but difficult to realize. Here, we report a new phenomenon that active intramolecular motions could promote PA signal by specifically increasing thermal-to-acoustic conversion efficiency. The compound with intense intramolecular motion exhibits amplified PA signal by elevating thermal-to-acoustic conversion, and the fluorescence also increases due to aggregation-induced emission signature. The simultaneously high PA and fluorescence brightness of TPA-TQ3 NPs enable precise image-guided surgery. The preoperative fluorescence and PA imaging are capable of locating orthotopic breast tumor in a high-contrast manner, and the intraoperative fluorescence imaging delineates tiny residual tumors. This study highlights a new design guideline of intramolecular motion amplifying PA effect.

Introduction

Photoacoustic (PA) imaging has attracted tremendous attention for biomedical applications as it offers centimeter-depth penetration and high spatial resolution (~100 μm) simultaneously by integrating the high contrast of optical imaging with the good penetration of ultrasound.^[1-4] For PA technique, a pulsed laser beam usually irradiates on the light-absorbing molecules or biospecies to produce localized thermal expansion, and then generate pressure changes as ultrasound wave.^[5-7] PA technique has been adopted for preclinical diagnosis of many diseases in vivo, for example, tumor imaging, inflammation and infection monitoring, and metastatic lymph node detection.^[8-13] It is highly desirable to develop high-contrast agents that are able to efficiently detect diseased site. Recently, organic/polymer chromophores have been used for PA imaging thanks to the facile synthesis and tunable material properties.^[14-17] However, how to realize maximal PA signal output is still a big challenge.

According to the Jablonski diagram, PA signal is mainly related to the thermal deactivation of a chromophore, while fluorescence emission derives from another energy dissipation pathway, i.e.,

radiative decay from the excited state to ground state.^[18-20] Therefore, it has been widely accepted that PA and fluorescence are opposite to or work against each other in one agent.^[21-24] Nevertheless, the intrinsic and complementary merits of PA and fluorescence techniques make the integration of them an optimal option for precise in vivo imaging by making full use of their advantages. For example, PA technique possesses high tissue penetration and spatial resolution, but suffers from relatively low sensitivity, while fluorescence imaging, on the other hand, has very high sensitivity but unsatisfied penetration.^[25-28] Thus, it's in great demand to obtain both high PA and fluorescence signals at the same time.

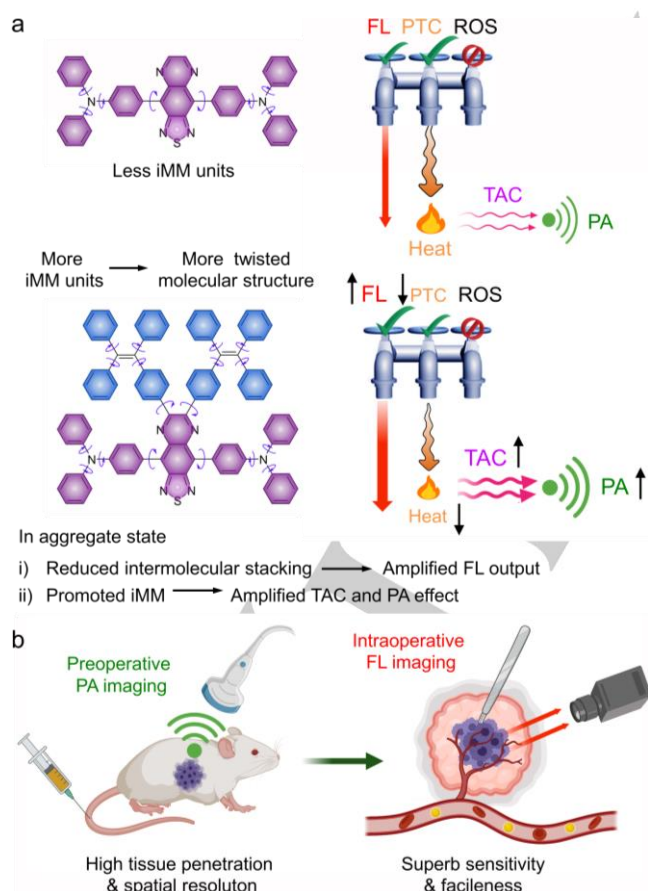
PA effect is closely related to two processes: photothermal conversion and subsequent thermal-to-acoustic transformation of a light-absorbing material.^[29] These processes can be described by the PA equation: $p = \Gamma\eta H$, where p is the PA pressure, Γ is the Grüneisen parameter, η is the energy supplied by a laser pulse, and H is the conversion efficiency from light into heat, or photothermal conversion efficiency (PCE).^[30-33] So far, intensive investigations have focused on elevating PCE to improve PA effect, yet the thermal-to-acoustic conversion efficiency or Grüneisen parameter is seldom considered. The investigation on thermal-to-acoustic conversion process may represent a new way for maximizing PA signal. Grüneisen parameter is a key factor responsible for the thermoelastic efficiency of materials, which decidedly links to the molecular structure.^[34,35] The understanding and manipulation of Grüneisen parameter from molecular level is thus of critical significance to boost PA effect and PA imaging performance. To the best of our knowledge, nevertheless, such studies are rare.

Molecular motion determines the basic properties of matter as all macroscopic nature can be traced back to the microscopic molecular motion.^[36,37] How to tune and utilize the active molecular motion is vitally important for both fundamental researches and practical applications. For instance, molecular machine has become a hot research topic in recent years because it is expected to bring revolutions in many aspects of technology and medicine.^[38-41] A basic thermal expansion principle that most matter expands when heated and contracts when cooled can also be traced back to microcosmic molecular

RESEARCH ARTICLE

motion, in which the thermal expansion process is related to Grüneisen parameter.^[42,43] Therefore, manipulation of the intramolecular motion is of critical importance as it greatly impacts the photophysical energy transformation processes. Recently, we and other groups reported that intramolecular motion could effectively enhance PCE, which favors the related applications such as photothermal therapy.^[44-47] Nevertheless, the influence of intramolecular motion on thermal-to-acoustic transformation process has never been explored thus far, which may represent a new way to tune PA property.

In this contribution, we demonstrate for the first time that intramolecular motion could promote PA effect by amplifying thermal-to-acoustic conversion, significantly benefitting the biomedical applications (Scheme 1). By comparing the PA signal of several analogs with different molecular rotors, we find that both PA and fluorescence intensity enhance by increasing active intramolecular motion, which is quite different from previous point of view that fluorescence and PA are competitive processes. Further investigation on the photothermal and PA transition suggests that the active intramolecular motion is capable of elevating Grüneisen parameter and thermal-to-acoustic conversion. As a proof-of-concept, the optimal agent has been used for precise image-guided surgery in orthotopic 4T1 breast tumor-bearing mice. The preoperative fluorescence imaging helps to localize tumor site in a fast way, and PA imaging further provides detailed information such as tumor geometry and depth, which offer unambiguous guidance for conducting surgery.



Scheme 1. Schematic illustrations of (a) intramolecular motions (iMM) amplifying fluorescence (FL) as well as thermal-to-acoustic conversion (TAC) and PA effect, benefitting for (b) adaptive image-guided cancer surgery by preoperative PA imaging and intraoperative FL imaging. PTC: photothermal conversion; ROS: reactive oxygen species.

Moreover, the intraoperative fluorescence imaging helps to delineate tiny residual tumors in a sensitive and fast manner, greatly improving the surgery outcome. This work brings up a new concept that the intense intramolecular motion helps to boost thermal-to-acoustic transition and thus advances PA imaging and complicated biomedical applications.

Results and Discussion

Design, Synthesis and Calculation. To obtain low-bandgap chromophore with near-infrared (NIR) absorption, donor-acceptor (D-A) strategy was employed, in which triphenylamine (TPA) and thiadiazoloquinoxaline (TQ) were used as the D and A moieties, respectively. In order to investigate the influence of intramolecular motion on the PA property of organic chromophore, a series of compounds based on the structure of “TPA-TQ-TPA” with different substituted groups in TQ core were synthesized. As shown in Figure 1a, the substituted groups in TPA-TQ1–3 were hydrogen, phenyl, and tetraphenylethylene (TPE), respectively. From TPA-TQ1 to TPA-TQ3, the intramolecular motion was expected to increase in order. TPE is a popularly used building block for constructing aggregation-induced emission (AIE) luminogens due to its highly twisted structure.^[48-50] Furthermore, the free rotation and vibration nature of TPE would also allow more space for the molecular motions in solid/aggregate state. The synthetic route of these compounds was depicted in Scheme S1, and the detailed synthetic processes and characterizations of the intermediates and final products were presented in Supporting Information (Figures S1-S12).

Density functional theory (DFT) calculation was employed to investigate the molecular geometry and electron cloud distribution. As shown in Figure 1b, the optimized molecular geometry became more twisted from TPA-TQ1 to TPA-TQ3 due to the introduction of molecular rotors. Noteworthy, TPA-TQ3 possessed a twisted 3D geometry with a severely distorted structure, which enabled more intense intramolecular motions. The lowest unoccupied molecular orbital (LUMO) energy level was located in the A part, while the highest occupied molecular orbital (HOMO) distributed in both D and A moieties (Figure S13), suggesting efficient intramolecular charge transfer. Moreover, the distribution of electron cloud in the phenyl rings attached to pyrazine of TPA-TQ2 and TPA-TQ3 indicated extended conjugation. As revealed by the X-ray diffraction (XRD) analysis (Figure 1c), the powder crystallinity decreased from TPA-TQ1 to TPA-TQ3, indicating that the molecular geometry had great impact on the intermolecular interaction in aggregate state. The increased intermolecular distance and space of TPA-TQ3 (Figure 1d) would allow more intense intramolecular motions, which was expected to alter the photophysical properties and optical imaging performance.

Photophysical Properties. The absorption spectra of TPA-TQ1–3 in THF were shown in Figure S14, and the absorption maxima were located at 587, 609, and 614 nm (Table S1), respectively. The gradual bathochromic shift originated from the contribution of phenyl and TPE to the molecular conjugation. Similarly, the photoluminescence (PL) profiles also exhibited red shift (Figure S15), but not as pronounced as the absorption. In order to gain in-depth understanding about the photophysical properties, the PL spectra in different aggregate states were studied by adding water (poor solvent) into THF (good solvent) solution. The PL intensity decreased gradually from 0% to 50% or

RESEARCH ARTICLE

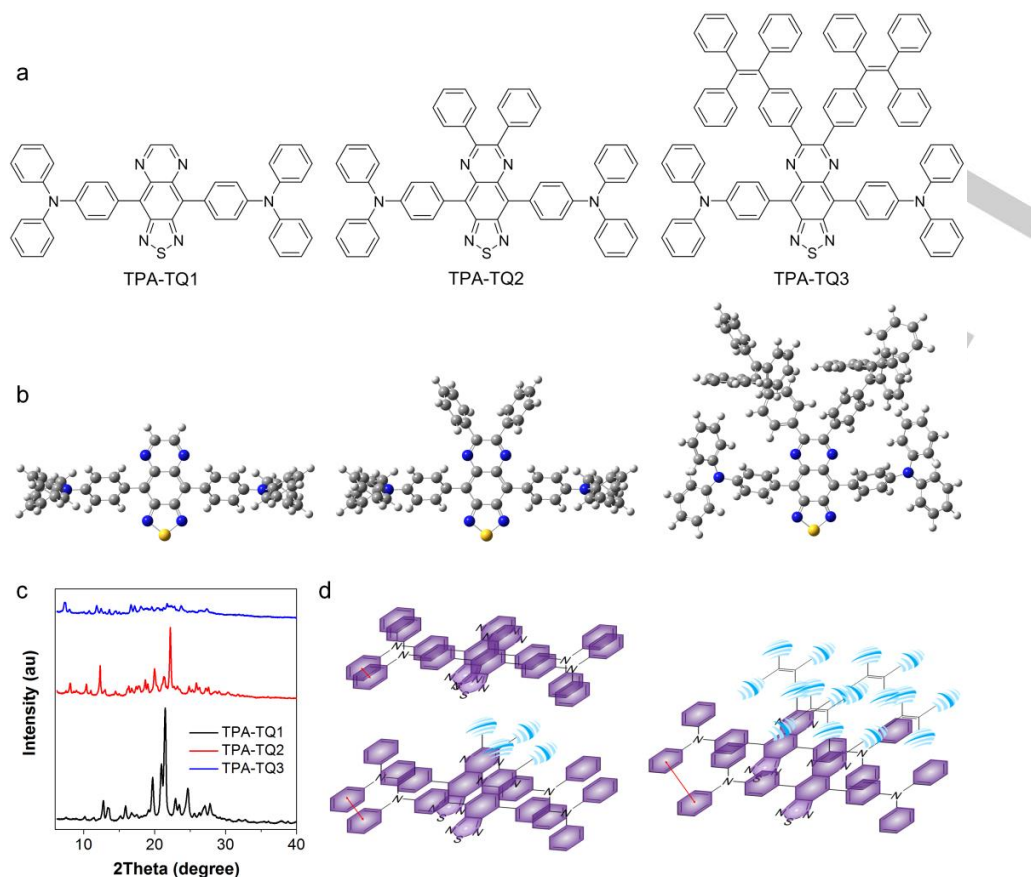


Figure 1. (a) Chemical structures, (b) optimized molecular geometry, (c) XRD diagrams of the powders, and (d) schematic intermolecular distance of TPA-TQ1–3.

60% water fraction, which could be attributed to the increased polarity and formation of twisted intramolecular charge transfer (TICT) state.^[51,52] The PL intensified when further increasing the water fraction (Figure S16), demonstrating obvious AIE signature. Interestingly, the enhancement of PL intensity in aggregate state increased from TPA-TQ1 to TPA-TQ3, which could be assigned to the more twisted molecular structure, and therefore reduced intermolecular interaction such as π - π stacking.

To understand the intermolecular interactions in aggregate state, molecular dynamics (MD) simulations of TPA-TQ1 and TPA-TQ3 were carried out using the GROMACS program.^[53,54] The snapshots were picked from the production simulations to show the packing manner of the molecules in aggregate. As displayed in Figure 2a,b, both TPA-TQ1 and TPA-TQ3 aggregates exhibited amorphous forms in disordered manners, which caused relatively loose packing. Additionally, the intramolecular motions in aggregates were still active but partially restricted due to the surrounding loosely packed molecules. To demonstrate the microscopic dynamics in atomic resolution, several key dihedral angle distributions were recorded (Figure 2c,d). It was found that the distributions of dihedral angles D1, D2 and D3 of TPA-TQ1 and TPA-TQ3 were similar, in which D2 and D3 had wider distributions than D1, implying more flexible feature of the phenyl rings in D2 and D3. Moreover, TPA-TQ3 had additional rotors, like D4, D5 and D6 in TPE moieties, which possessed wide distribution range, leading to reduced intermolecular interaction and intensive intramolecular motions.

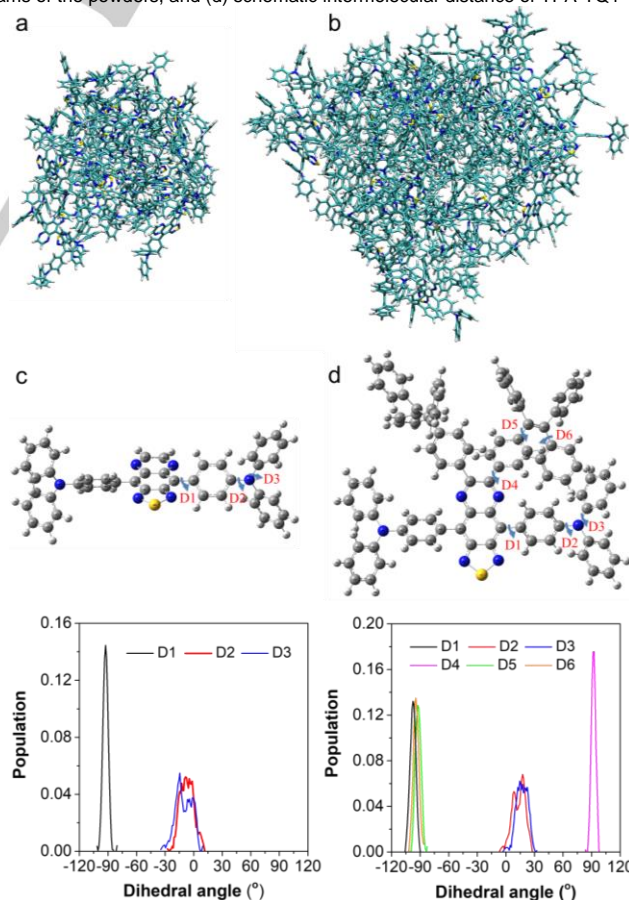


Figure 2. Snapshots of the amorphous aggregates of (a) TPA-TQ1 and (b) TPA-TQ3 obtained from molecular dynamics simulation. Different dihedral angles distributions of (c) TPA-TQ1 and (d) TPA-TQ3 in aggregate state.

RESEARCH ARTICLE

Fabrication and Characterization of Nanoparticles. To study the optical imaging property in aggregate state and explore biomedical applications, the compounds were doped into water-soluble nanoparticles (NPs) with a nanoprecipitation method. The amphiphilic polymer 1,2-distearoyl-*sn*-glycero-3-phosphoethanolamine-*N*-[methoxy-(polyethylene glycol)-2000] (DSPE-PEG₂₀₀₀) was adopted as the encapsulation matrix and the hydrophobic organic molecules self-assembled in the core. Dynamic light scattering (DLS) measurements indicated that the average diameters of TPA-TQ1–3 NPs were in sequence 73, 75, and 80 nm, and the transmission electron microscope (TEM) results revealed that the NPs were approximate sphere structures with diameters of about 70 nm (Figures 3a and Figure S17). The absorption profiles showed strong absorption in the spectral region of 550–750 nm (Figure 3b), which could be excited by the pulsed laser of commercially available PA instrument. TPA-TQ1–3 NPs displayed PL spectra in the range of 700–1200 nm with maxima at about 820 nm (Figure 3c), in which the broad emission

could be attributed to the conformational variation from twisted molecular geometry.^[55,56] The large Stokes shift of about 200 nm could efficiently avoid the overlap between absorption and emission spectra, enabling full utilization of the emission light. PL excitation (PLE) mapping (Figure 3d and Figures S18,S19) further revealed that both the excitation and emission of the nanoagents were located in NIR region. The PL quantum yield (PLQY) of TPA-TQ1–3 NPs was measured to be 1.4%, 3.9%, and 6.8% using an integrating sphere (Figure 3e), which were in accordance with the differences of AIE property. The increased fluorescence brightness from TPA-TQ1 NPs to TPA-TQ3 NPs was probably because the large twisted molecular structure could inhibit intermolecular quenching effect, and thus facilitate the radiative decay. The brightness had also been confirmed by the images from *in vivo* imaging system (IVIS) (Figure 3e). Noteworthy, PLQY of TPA-TQ3 NPs (6.8%) represented a high value among organic fluorophores with similar emission wavelength in aggregate state.

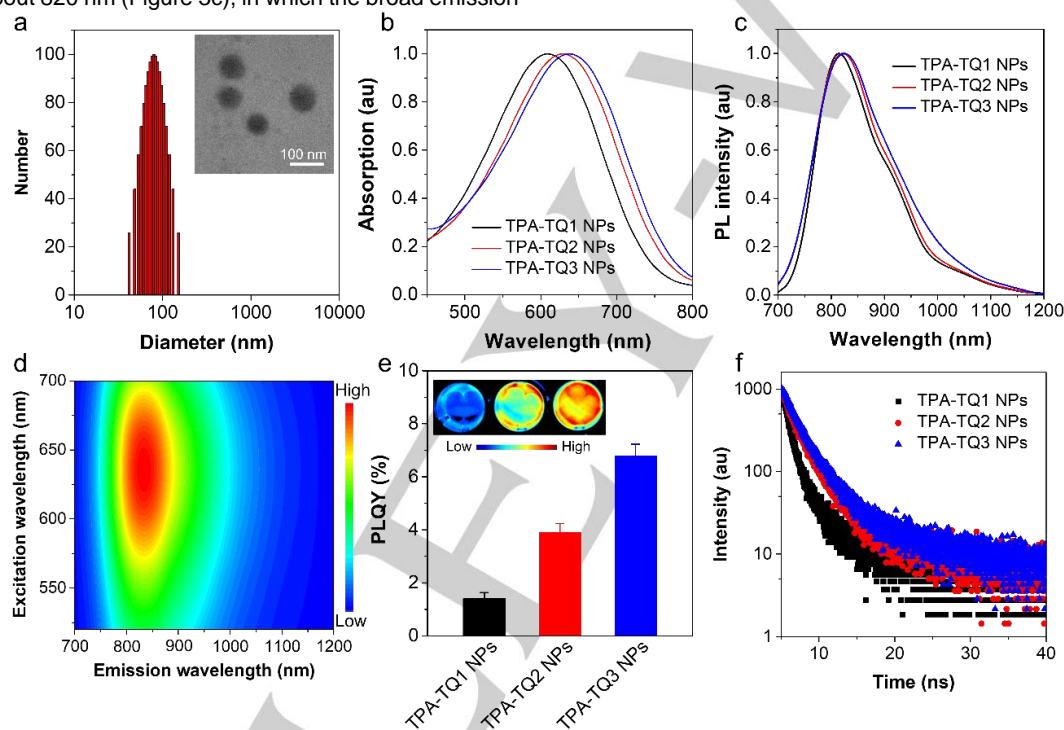


Figure 3. (a) Representative DLS and TEM results of TPA-TQ3 NPs. (b) Absorption and (c) PL spectra of TPA-TQ1–3 NPs, respectively. (d) PLE mapping of TPA-TQ3 NPs. (e) PLQY values of TPA-TQ1–3 NPs. Data are presented as mean \pm s.d. ($n = 3$). Inset shows the brightness images of various NPs solution obtained from IVIS. (f) Fluorescence decay curves of TPA-TQ1–3 NPs.

In order to gain in-depth understanding about the photophysical transition processes, we measured the fluorescence lifetime of various NPs. The lifetime (τ) increased from TPA-TQ1 NPs to TPA-TQ3 NPs, which was in the same trend as PLQY (Figure 3f). The fluorescence properties were closely related to the radiative and non-radiative decay rates (k_r and k_{nr}).^[57–59] According to the equations: $\tau = 1/(k_r + k_{nr})$, $\Phi_F = k_r/(k_r + k_{nr})$, the k_r/k_{nr} values of TPA-TQ1–3 NPs were calculated to be $0.136/9.57 \times 10^8$, $0.215/5.31 \times 10^8$ and $0.287/3.93 \times 10^8 \text{ s}^{-1}$ (Table S1), respectively. Interestingly, the radiative decay increased gradually from TPA-TQ1 to TPA-TQ3 NPs, meanwhile the non-radiative decay decreased. This result revealed that the non-radiative decay process of the highly twisted structure was greatly inhibited and the radiative decay was enhance in aggregate form.

Photothermal and PA Properties. The PA spectra of TPA-TQ1–3 NPs were measured by recording the PA intensity at

different wavelengths from 680 to 800 nm. As shown in Figure 4a, the PA spectra matched well with the absorption profile, which suggested that the PA signal originated from the absorption of the NIR chromophores. Interestingly, TPA-TQ3 NPs exhibited the highest PA intensity, which was more than two-fold higher than TPA-TQ1 NPs and 1.7 times higher than TPA-TQ2 NPs. Thus, TPA-TQ3 NPs displayed both high fluorescence and PA signal, which was different from previous reports that the PA and fluorescence transition processes of one agent work against each other.^[60,61] To further validate this phenomenon, the PA amplitudes of the NPs in different concentrations were measured. As displayed in Figure 4b,c, the PA intensity also increased in the order of TPA-TQ3 NPs > TPA-TQ2 NPs > TPA-TQ1 NPs, and the PA amplitude showed very good linear relationship with the concentration, indicating good stability and great potential for quantitative analysis. Furthermore, the comparison of PA amplitude of TPA-TQ1–3 NPs and the popularly used methylene

RESEARCH ARTICLE

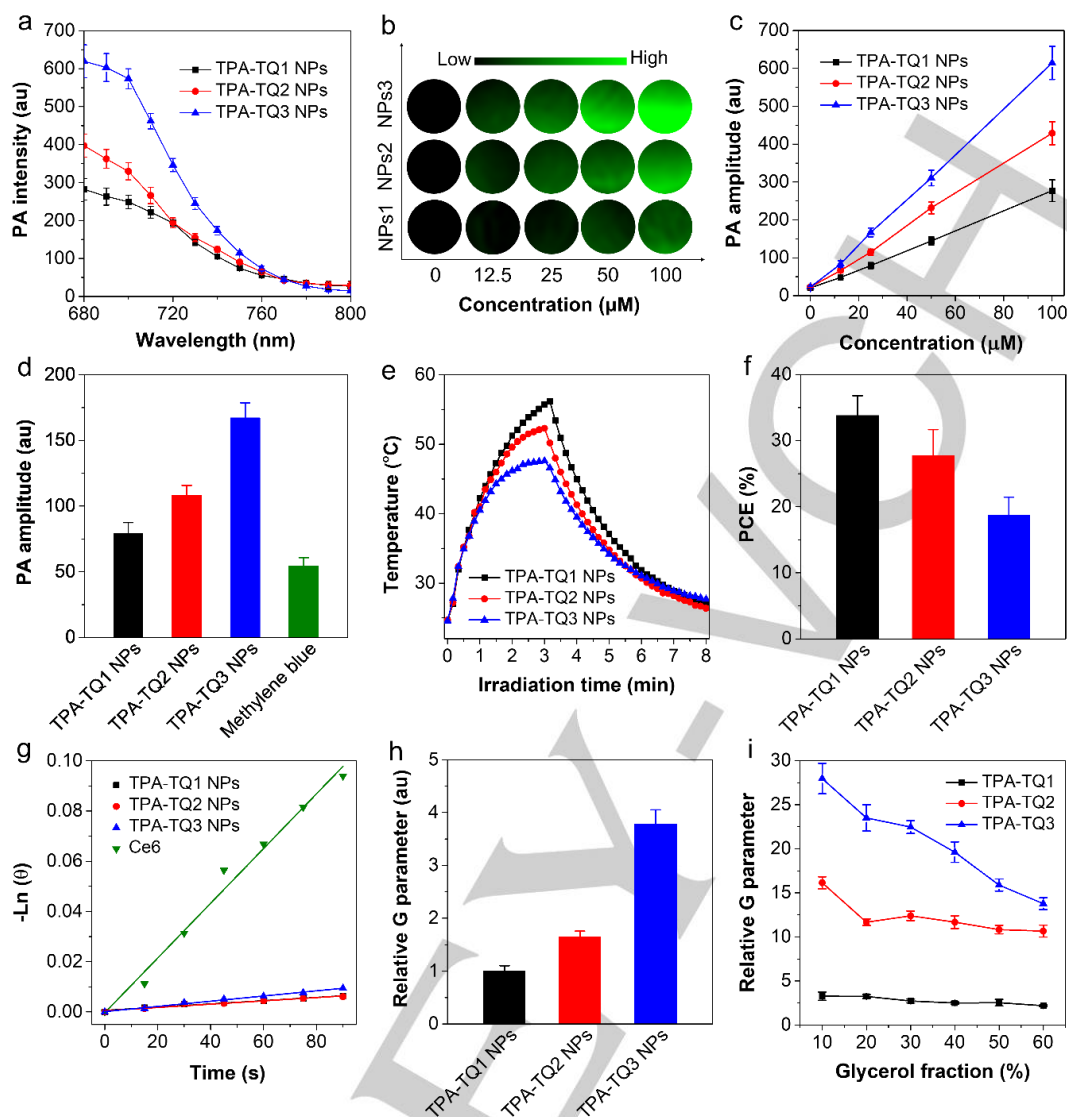


Figure 4. (a) PA spectra of TPA-TQ1–3 NPs. (b) PA images and (c) corresponding PA amplitude versus the concentration of NPs. (d) PA amplitude of TPA-TQ1–3 NPs and methylene blue in the same concentration (50 μM) at 680 nm. (e) Photothermal heating–cooling process and (f) PCE of TPA-TQ1–3 NPs under continuous irradiation of 660 nm light (0.4 W/cm²). (g) ROS generation property of TPA-TQ1–3 NPs and chlorin e6 (Ce6) under light irradiation. (h) Relative Grüneisen parameters of TPA-TQ1–3 NPs solution. (i) Relative Grüneisen parameters of TPA-TQ1–3 in DMF/glycerol mixture with different glycerol fractions. Data are presented as the means ± s.d. (*n* = 3).

blue (MB) in the same concentration (50 μM) with 680 nm pulsed laser excitation (Figure 4d) indicated that the PA intensity of TPA-TQ1–3 NPs were in sequence 1.6, 2.1, and 3.5 times higher than that of MB, illustrating that TPA-TQ3 NPs were a highly potent PA contrast agent.

To study the origination of the highest PA signal of TPA-TQ3 NPs among all NPs, we first investigated their photothermal property. Under the same light irradiation for 3 min, the highest temperatures that TPA-TQ1–3 NPs solution could be reached were 56.2, 52.3 and 47.6 °C (Figure 4e), respectively. The PCE values of TPA-TQ1–3 NPs were calculated to be 33.8%, 27.8%, and 18.7% (Figure 4f), respectively. The decrease of PCE from TPA-TQ1 NPs to TPA-TQ3 NPs was consistent with the reduced non-radiative decay. This result also manifested that PLQY and PCE were competitive as they directly corresponded to the radiative and non-radiative decay processes of Jablonski diagram. We also studied other possible energy dissipation pathways such as phosphorescence and photosensitization in the triplet excited state, but no obvious related processes could be detected for TPA-TQ1–3 NPs (Figure 4g). As PA effect is closely related to

both the photothermal conversion and subsequent thermal-to-acoustic transformation processes, and the decreased PCE could not explain the high PA signal of TPA-TQ3, thus the thermal-to-acoustic conversion property of TPA-TQ1–3 NPs solution was studied. Since the same excitation pulsed laser was used, Grüneisen parameters could be estimated from the aforementioned PA equation. As displayed in Figure 4h, the relative Grüneisen parameters of TPA-TQ2 NPs and TPA-TQ3 NPs were about 1.5- and 4-fold higher than that of TPA-TQ1 NPs. To further understand the influence of intramolecular motion on PA generation process, the PA amplitude, PCE and Grüneisen parameter of TPA-TQ1–3 in the mixture of *N,N*-dimethylformamide (DMF) and glycerol with different glycerol fractions were measured. The increase of glycerol fraction could result in viscous environment and restrict the intramolecular motions. The results revealed that the relative Grüneisen parameters of TPA-TQ1 and TPA-TQ2 hardly changed with viscosity. While the relative Grüneisen parameters of TPA-TQ3 decreased for about 50% in the solution with 60% glycerol (Figure 4i), probably due to the highly restricted molecular motion in high-viscosity environment. This result suggested that the Grüneisen

RESEARCH ARTICLE

parameter and related thermal-to-acoustic transformation were greatly impacted by the intramolecular motions. The free molecular rotations and vibrations were able to promote the PA signal via amplifying Grüneisen parameter or thermal-to-acoustic conversion. This finding also demonstrated a new strategy to simultaneously obtain high PA and fluorescence brightness in one chromophore.

After demonstrating that active intramolecular motion could promote thermo-to-acoustic conversion, we next sought to validate whether this molecular design could be extended to other system. In this case, two D-A type compounds based on TPA and thienothiadiazole (TT) were designed and synthesized (Scheme S2, Figures S21-S26), in which either hydrogen or TPE was chosen as the substituted group. As expected, the TPE-containing compound (TPE-TPA-TT) exhibited more twisted molecular geometry, and it also possessed more pronounced AIE feature and reduced crystallinity, when compared with its analog (TPA-TT) (Figure 5a,b and Figures S27,S28). The fluorescence and PA properties of TPA-TT and TPE-TPA-TT NPs were further compared. The results showed that TPE-TPA-TT NPs exhibited much higher PLQY and stronger PA signal than TPA-TT NPs. And the calculated relative Grüneisen parameter of TPE-TPA-TT NPs solution was nearly three times greater than that of TPA-TT NPs (Figure 5c,d and Figures S29,S30). This result suggested that TPE-TPA-TT with violent intramolecular motion showed higher thermo-to-acoustic conversion efficiency thanks to the violent intramolecular motion. Accordingly, the introduction of intramolecular motion is an effective strategy to promote thermal-to-acoustic conversion and thus PA signal.

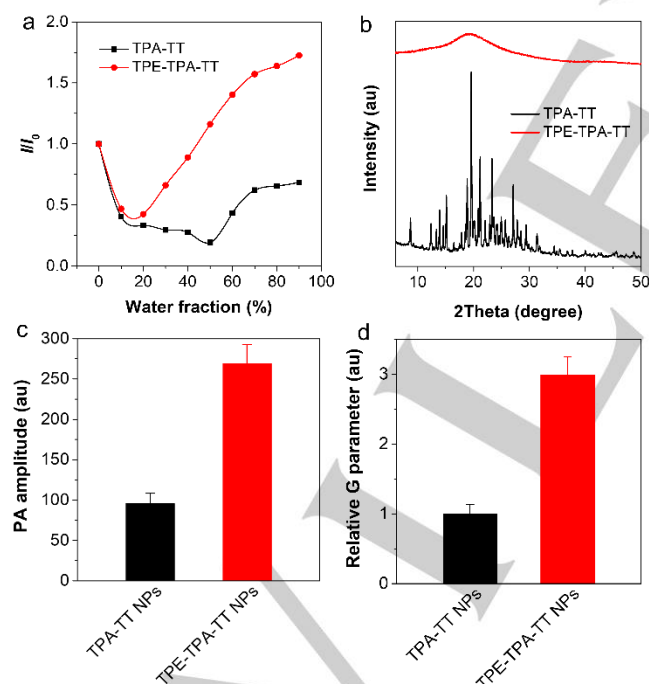


Figure 5. (a) Plot of PL peak intensity of TPA-TT and TPE-TPA-TT versus water fraction (f_w) in THF/water mixtures (2×10^{-5} M). I_0 and I represent the PL intensities of the compounds in pure THF ($f_w = 0$) and THF/water mixtures with specific f_w s. (b) XRD diagrams of TPA-TT and TPE-TPA-TT powders. (c) PA amplitude of TPA-TT NPs and TPE-TPA-TT NPs in the same concentration (50 μ M) at 680 nm. (d) Relative Grüneisen parameters of TPA-TT NPs and TPE-TPA-TT NPs solution. Data are presented as the means \pm s.d. ($n = 3$)

In Vivo Image-Guided Tumor Surgery. Precise image-guided surgery calls for high-performance imaging techniques that meet the requirements during the whole operation process.^[62,63] To

improve both surgical outcomes and patient safety, different imaging modalities usually need to be combined to gain comprehensive information of the lesion in different stages.^[64,65] The excellent PA and fluorescence properties of TPA-TQ3 NPs make it a suitable candidate for in vivo biomedical applications. To test their potential use for image-guided surgery, the TPA-TQ1-3 nanoprobes were injected into the mice bearing orthotopic 4T1 breast tumor through tail veins, and the fluorescence and PA images were recorded at designed time intervals. The live-animal fluorescence and PA imaging were then performed for pre-surgery diagnosis. As presented in Figure 6a,b, the in vivo fluorescence intensity of tumor sites gradually intensified as time elapse and became highest at about 8 h post-injection, suggesting the optimal time to perform in vivo imaging. Noteworthy, the fluorescence intensity of the tumor site of TPA-TQ3 NPs-treated mice was about 3.1-fold and 1.9-fold stronger than that of TPA-TQ2 NPs and TPA-TQ1 NPs, respectively, which was in line with the PLQY results. With the high fluorescence brightness, TPA-TQ3 NPs significantly lighted up the tumor tissue and clearly delineated tumor from surrounding normal tissues. The ex vivo imaging of the main organs and tumor resected from the mice injected with TPA-TQ3 NPs for 24 h (Figure S31) also revealed that the tumor tissue displayed very high fluorescence signal, which benefited from the high PLQY of TPA-TQ3 NPs as well as its potent tumor accumulation mediated by the enhanced permeability and retention (EPR) effect.^[66,67] In the meantime, the mice were also imaged with PA instruments under 700 nm pulsed laser excitation. After intravenous administration of TPA-TQ3 NPs, the PA signal of tumor site could be clearly observed at 3 h post injection and reached highest at 8 h post injection. The PA signal of tumor at 8 h was elevated by 7.3 folds when compared with that at 0 h. Such result was even better than most reported high-performance PA agents.^[60,68] By making full use of the high sensitivity and facile equipment of fluorescence technique and good penetration ability and spatial resolution of PA imaging, the TPA-TQ3 NPs-based combined preoperative imaging strategy provided comprehensive information about tumor, rendering the surgeon advantageous guidance on surgical plan.

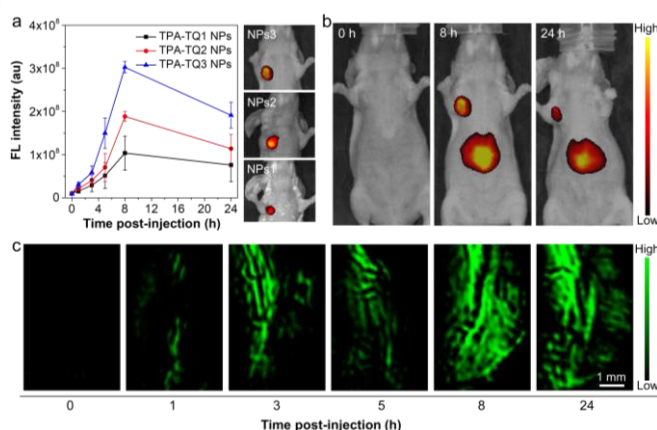


Figure 6. (a) Fluorescence intensity of the tumor site as a function of post-injection time and representative fluorescence images of mice bearing orthotopic 4T1 breast tumor at 8 h post injection of TPA-TQ1-3 NPs. Data are presented as the means \pm s.d. ($n = 3$ mice per group). Representative (b) fluorescence and (c) PA images of mice bearing orthotopic 4T1 breast tumor after intravenous injection of TPA-TQ3 NPs at different time intervals as indicated.

Tumor resection was then conducted by a surgeon from Tianjin First Central Hospital (Tianjin, China) with the information

RESEARCH ARTICLE

provided by preoperative fluorescence and PA imaging. The most challenging problem during cancer surgery is the differentiation of tiny residual tumors as they are really difficult to recognize by naked eyes.^[69] The high sensitivity and equipment flexibility of fluorescence imaging make it an ideal option for rapid intraoperative imaging, which has also been used in clinic.^[70,71] As indicated in Figure 7a, the intraoperative NIR fluorescence imaging enabled unambiguous detection of tiny tumor tissues in real time. The fluorescence signal was found to be in good accordance with the bioluminescence from the luciferase-expressed tumor cells, which confirmed that the fluorescently labelled areas were indeed tumor tissue. The residual tumor nodules identified by fluorescence imaging were also examined with hematoxylin and eosin (H&E) histological analysis (Figure S33), implying those were tiny tumors of < 500 μm in size. With the guidance of fluorescence imaging, the second surgery was carried out to resect all residual orthotopic breast tumor nodules until no NIR fluorescence signal could be observed. To examine the validity of this integrated surgery imaging strategy, survival rate study was conducted on several groups: the orthotopic 4T1 breast tumor-bearing mice without any surgery (Control), with residual tumors from intraoperative NIR fluorescence imaging (S1), and excision of residual tumors until no intraoperative NIR fluorescence signal (S2). The mice in the Control and S1 groups were all died within 40 days. In contrast, only one mouse in S2 group was died on day 31 post-surgery, and all other mice were survival in the 45-days duration (Figure 7b). The significantly increased survival rate in S2 group manifested the great advantage of TPA-TQ3 NPs for integrated imaging in different surgical stages. This work validated that the optical imaging agent developed here with both excellent fluorescence and PA properties could serve as a potent probe for tumor resection guidance by combining the preoperative fluorescence/PA and intraoperative fluorescence imaging.

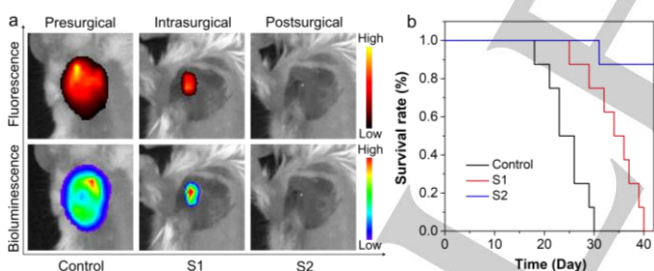


Figure 7. (a) Representative pre-, intra- and post-surgical fluorescence/bioluminescence images of orthotopic 4T1 breast tumors. (b) Survival curves of orthotopic 4T1 breast tumor-bearing mice received various treatments ($n = 8$ mice per group).

Biocompatibility was of critical significance for the in vivo applications of optical imaging agents, so we investigated the in vitro and in vivo safety of TPA-TQ3 NPs. The cytotoxicity was first evaluated by co-culturing different concentrations (0, 2, 5, 10, 25, 50 μM) of TPA-TQ1-3 NPs with 4T1 cancer cells. As shown in Figure S34, the cell viability was higher than 90% with the treatment of a high concentration (50 μM), indicating low cytotoxicity of the NPs. TPA-TQ3 NPs were then injected into healthy mice to examine the in vivo biosafety. The hepatic and renal function analyses (Figure S35) and blood routine examination (Figure S36) of the TPA-TQ3 NPs-treated mice showed no noticeable abnormalities. In addition, the H&E staining of the major organs, including heart, liver, spleen, lung, and kidney did not show any notable pathological changes 7 days

after NPs injection (Figure S37). Taken together, these results revealed that the organic NPs had good biocompatibility and no obvious side effect was observed.

Conclusion

In summary, we demonstrated for the first time that intramolecular motion represented an efficient strategy to amplify PA signal, in particular the thermal-to-acoustic conversion process. By introducing molecular rotor-rich unit (e.g., TPE), both the fluorescence and PA properties were improved. The underlying mechanism was also investigated, which demonstrated that the twisted conformations of the rotor-rich compounds were favorable for AIE property and high fluorescence brightness, and intramolecular motion promoted the thermal-to-acoustic conversion process to achieve outstanding PA signal. The simultaneously high PA and fluorescence imaging properties warranted TPA-TQ3 NPs a superb probe for in vivo biomedical applications. The preoperative NIR fluorescence/PA imaging helped to localize tumor site, geometry and depth of orthotopic 4T1 breast tumor-bearing mice in a high-contrast manner, providing unambiguous guidance for performing surgery. Furthermore, the intraoperative NIR fluorescence imaging enabled the delineation of tiny residual tumors in a fast and sensitive way, significantly boosting the surgery outcome. This work demonstrated that intramolecular motion represented a new approach to amplify PA signal by increasing the thermal-to-acoustic conversion, greatly advancing complicated biomedical applications.

Acknowledgements

This work was supported by the National Natural Science Foundation of China (51873092, 51961160730 and 21803007), the National Key R&D Program of China (Intergovernmental cooperation project, 2017YFE0132200), Tianjin Science Fund for Distinguished Young Scholars (19JCJQC61200), and Beijing Institute of Technology (BIT) Research Fund Program for Young Scholar.

Conflict of interest

The authors declare no conflict of interest.

Keywords: intramolecular motion • thermal-to-acoustic conversion • photoacoustic • aggregation-induced emission • image-guided surgery

- [1] L.V. Wang, S. Hu, *Science* **2012**, *335*, 1458–1462.
- [2] K. Pu, A. J. Shuhendler, J. V. Jokerst, J. Mei, S. S. Gambhir, Z. Bao, J. Rao, *Nat. Nanotechnol.* **2014**, *9*, 233–239.
- [3] J. Weber, P.C. Beard, S. E. Bohndiek, *Nat. Methods* **2016**, *13*, 639–650.
- [4] C. Zhou, L. Zhang, T. Sun, Y. Zhang, Y. Liu, M. Gong, Z. Xu, M. Du, Y. Liu, G. Liu, D. Zhang, *Adv. Mater.* **2021**, *33*, 2006532.
- [5] C. Kim, C. Favazza, L. V. Wang, *Chem. Rev.* **2010**, *110*, 2756–2782.
- [6] J. Qi, L. Feng, X. Zhang, H. Zhang, L. Huang, Y. Zhou, Z. Zhao, X. Duan, F. Xu, R. T. K. Kwok, J. W. Y. Lam, D. Ding, X. Xue, B. Z. Tang, *Nat. Commun.* **2021**, *12*, 960.

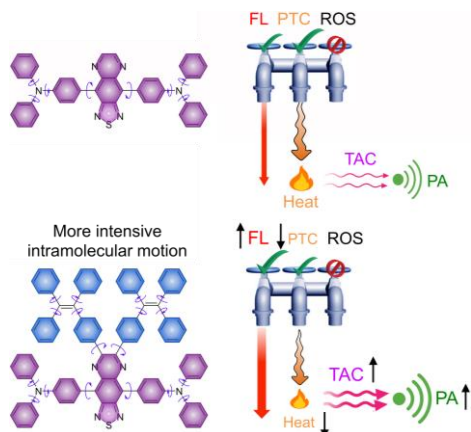
RESEARCH ARTICLE

- [7] S. Jeon, J. Kim, D. Lee, J. W. Baik, C. Kim, *Photoacoustics* **2019**, *15*, 100141.
- [8] L. V. Wang, J. Yao, *Nat. Methods* **2016**, *13*, 627–638.
- [9] Q. Fan, K. Cheng, Z. Yang, R. Zhang, M. Yang, X. Hu, X. Ma, L. Bu, X. Lu, X. Xiong, W. Huang, H. Zhao, Z. Cheng, *Adv. Mater.* **2015**, *27*, 843–847.
- [10] J. Qi, J. Li, R. Liu, Q. Li, H. Zhang, J. W. Y. Lam, R. T. K. Kwok, D. Liu, D. Ding, B. Z. Tang, *Chem* **2019**, *5*, 2657–2677.
- [11] X. Ai, Z. Wang, H. Cheong, Y. Wang, R. Zhang, J. Lin, Y. Zheng, M. Gao, B. Xing, *Nat. Commun.* **2019**, *10*, 1087.
- [12] H. Wang, J. Chang, M. Shi, W. Pan, N. Li, B. Tang, *Angew. Chem. Int. Ed.* **2019**, *58*, 1057–1061.
- [13] Z. Wang, X. Zhen, P. K. Upputuri, Y. Jiang, J. Lau, M. Pramanik, K. Pu, B. Xing, *ACS Nano* **2019**, *13*, 5816–5825.
- [14] J. F. Lovell, C. S. Jin, E. Huynh, H. Jin, C. Kim, J. L. Rubinstein, W. C. W. Chan, W. Cao, L. V. Wang, G. Zheng, *Nat. Mater.* **2011**, *10*, 324–332.
- [15] J. Li, K. Pu, *Chem. Soc. Rev.* **2019**, *48*, 38–71.
- [16] A. S. Jeevarathinam, J. E. Lemaster, F. Chen, E. Zhao, J. V. Jokerst, *Angew. Chem. Int. Ed.* **2020**, *59*, 4678–4683.
- [17] E. Y. Zhou, H. J. Knox, C. Liu, W. Zhao, J. Chan, *J. Am. Chem. Soc.* **2019**, *141*, 17601–17609.
- [18] H.-B. Cheng, Y. Li, B. Z. Tang, J. Yoon, *Chem. Soc. Rev.* **2020**, *49*, 21–31.
- [19] Y. Liu, P. Bhattarai, Z. Dai, X. Chen, *Chem. Soc. Rev.* **2019**, *48*, 2053–2108.
- [20] D. Wang, M. M. S. Lee, W. Xu, G. Shan, X. Zheng, R. T. K. Kwok, J. W. Y. Lam, X. Hu, B. Z. Tang, *Angew. Chem. Int. Ed.* **2019**, *58*, 5628–5632.
- [21] K. Li, B. Liu, *Chem. Soc. Rev.* **2014**, *43*, 6570–6597.
- [22] X. Ai, C. J. H. Ho, J. Aw, A. B. E. Attia, J. Mu, Y. Wang, X. Wang, Y. Wang, X. Liu, H. Chen, M. Gao, X. Chen, E. K. L. Yeow, G. Liu, M. Olivo, B. Xing, *Nat. Commun.* **2016**, *7*, 10432.
- [23] L. Xie, X. Pang, X. Yan, Q. Dai, H. Lin, J. Ye, Y. Cheng, Q. Zhao, X. Ma, X. Zhang, G. Liu, X. Chen, *ACS Nano* **2020**, *14*, 2880–2893.
- [24] X. Li, E.-Y. Park, Y. Kang, N. Kwon, M. Yang, S. Lee, W. J. Kim, C. Kim, J. Yoon, *Angew. Chem. Int. Ed.* **2020**, *59*, 8630–8634.
- [25] J. Qi, C. Chen, X. Zhang, X. Hu, S. Ji, R. T. K. Kwok, J. W. Y. Lam, D. Ding, B. Z. Tang, *Nat. Commun.* **2018**, *9*, 1848.
- [26] Kenry, Y. Duan, B. Liu, *Adv. Mater.* **2018**, *30*, 1802394.
- [27] K. Cheng, H. Chen, C. H. Jenkins, G. Zhang, W. Zhao, Z. Zhang, F. Han, J. Fung, M. Yang, Y. Jiang, L. Xing, Z. Cheng, *ACS Nano* **2017**, *11*, 12276–12291.
- [28] L. Yang, J. Li, W. Pan, H. Wang, N. Li, B. Tang, *Chem. Commun.* **2018**, *54*, 3656–3659.
- [29] M. Xu, L. V. Wang, *Rev. Sci. Instrum.* **2006**, *77*, 041101.
- [30] L. V. Wang, H. Wu, Wiley-Interscience, Hoboken, 2007.
- [31] Y.-S. Chen, W. Frey, S. Kim, P. Kruijzinga, K. Homan, S. Emelianov, *Nano Lett.* **2011**, *11*, 348–354.
- [32] H. Aoki, M. Nijiri, R. Mukai, S. Ito, *Nanoscale* **2015**, *7*, 337–343.
- [33] X. Zhen, X. Feng, C. Xie, Y. Zheng, K. Pu, *Biomaterials* **2017**, *127*, 97–106.
- [34] D.-K. Yao, C. Zhang, K. Maslov, L. V. Wang, *J. Biomed. Opt.* **2014**, *19*, 017007.
- [35] T. Fukasawa, S. Noguchi, H. Shinto, H. Aoki, S. Ito, M. Ohshim, *Colloids and Surfaces A: Physicochem. Eng. Aspects* **2015**, *487*, 42–48.
- [36] H. Zhang, L. Du, L. Wang, J. Liu, Q. Wan, R. T. K. Kwok, J. W. Y. Lam, D. L. Phillips, B. Z. Tang, *J. Phys. Chem. Lett.* **2019**, *10*, 7077–7085.
- [37] W. Danowski, T. van Leeuwen, S. Abdolazadeh, D. Roke, W. R. Browne, S. J. Wezenberg, B. L. Feringa, *Nat. Nanotechnol.* **2019**, *14*, 488–494.
- [38] T. C. Südhof, *Nat. Med.* **2013**, *19*, 1227–1231.
- [39] G. De Bo, S. Gall, M. A. Y. Kuschel, J. De Winter, P. Gerbaux, D. A. Leigh, *Nat. Nanotechnol.* **2018**, *13*, 381–385.
- [40] Y. Yuan, C. Du, C. Sun, J. Zhu, S. Wu, Y. Zhang, T. Ji, J. Lei, Y. Yang, N. Gao, G. Nie, *Nano Lett.* **2018**, *18*, 921–928.
- [41] Z. Zhao, H. Zhang, J. W. Y. Lam, B. Z. Tang, *Angew. Chem. Int. Ed.* **2020**, *59*, 9888–9907.
- [42] M. Bönisch, A. Panigrahi, M. Stoica, M. Calin, E. Ahrens, M. Zehetbauer, W. Skrotzki, J. Eckert, *Nat. Commun.* **2017**, *8*, 1429.
- [43] S. Watanabe, K. Miyake, *Phys. Rev. B* **2019**, *99*, 035108.
- [44] Z. Zhao, C. Chen, W. Wu, F. Wang, L. Du, X. Zhang, Y. Xiong, X. He, Y. Cai, R. T. K. Kwok, J. W. Y. Lam, X. Gao, P. Sun, D. L. Phillips, D. Ding, B. Z. Tang, *Nat. Commun.* **2019**, *10*, 768.
- [45] X. Li, L. Liu, S. Li, Y. Wan, J.-X. Chen, S. Tian, Z. Huang, Y.-F. Xiao, X. Cui, C. Xiang, Q. Tan, X.-H. Zhang, W. Guo, X.-J. Liang, C.-S. Lee, *ACS Nano* **2019**, *13*, 12901–12911.
- [46] D. Xi, M. Xiao, J. Cao, L. Zhao, N. Xu, S. Long, J. Fan, K. Shao, W. Sun, X. Yan, X. Peng, *Adv. Mater.* **2020**, *32*, 1907855.
- [47] J.-S. Ni, X. Zhang, G. Yang, T. Kang, X. Lin, M. Zha, Y. Li, L. Wang, K. Li, *Angew. Chem. Int. Ed.* **2020**, *59*, 11298–11302.
- [48] J. Mei, N. L. C. Leung, R. T. K. Kwok, J. W. Y. Lam, B. Z. Tang, *Chem. Rev.* **2015**, *115*, 11718–11940.
- [49] D. Ding, K. Li, B. Liu, B. Z. Tang, *Acc. Chem. Res.* **2013**, *46*, 2441–2453.
- [50] F. Xia, J. Wu, X. Wu, Q. Hu, J. Dai, X. Lou, *Acc. Chem. Res.* **2019**, *52*, 3064–3074.
- [51] J. Qi, C. Sun, A. Zebibula, H. Zhang, R. T. K. Kwok, X. Zhao, W. Xi, J. W. Y. Lam, J. Qian, B. Z. Tang, *Adv. Mater.* **2018**, *30*, 1706856.
- [52] A. L. Antaris, H. Chen, S. Diao, Z. Ma, Z. Zhang, S. Zhu, J. Wang, A. X. Lozano, Q. Fan, L. Chew, M. Zhu, K. Cheng, X. Hong, H. Dai, Z. Cheng, *Nat. Commun.* **2017**, *8*, 15269.
- [53] B. Hess, C. Kutzner, D. van der Spoel, E. J. Lindahl, *Chem. Theory Comput.* **2008**, *4*, 435–447.
- [54] C. C. Gruber, J. J. Pleiss, *Comput. Chem.* **2011**, *32*, 600–606.
- [55] D. Li, W. Hu, J. Wang, Q. Zhang, X.-M. Cao, X. Ma, H. Tian, *Chem. Sci.* **2018**, *9*, 5709–5715.
- [56] B. Li, Z. Li, F. Guo, J. Song, X. Jiang, Y. Wang, S. Gao, J. Wang, X. Pang, L. Zhao, Y. Zhang, *ACS Appl. Mater. Interfaces* **2020**, *12*, 14233–14243.
- [57] Q. Peng, Q. Shi, Y. Niu, Y. Yi, S. Sun, W. Li, Z. Shuai, *J. Mater. Chem. C* **2016**, *4*, 6829–6838.
- [58] Z. Zhao, H. Nie, C. Ge, Y. Cai, Y. Xiong, J. Qi, W. Wu, R. T. K. Kwok, X. Gao, A. Qin, J. W. Y. Lam, B. Z. Tang, *Adv. Sci.* **2017**, *4*, 1700005.
- [59] J. Qi, X. Duan, Y. Cai, S. Jia, C. Chen, Z. Zhao, Y. Li, H.-Q. Peng, R. T. K. Kwok, J. W. Y. Lam, D. Ding, B. Z. Tang, *Chem. Sci.* **2020**, *11*, 8438–8447.
- [60] K. Pu, J. Mei, J. V. Jokerst, G. Hong, A. L. Antaris, N. Chatto-padhyay, A. J. Shuhendler, T. Kurosawa, Y. Zhou, S. S. Gambhir, Z. Bao, J. Rao, *Adv. Mater.* **2015**, *27*, 5184–5190.
- [61] H. Xiao, C. Wu, P. Li, W. Gao, W. Zhang, W. Zhang, L. Tong, B. Tang, *Chem. Sci.* **2017**, *8*, 7025–7030.
- [62] E. Y. Lukianova-Hleb, Y.-S. Kim, I. Belatskouski, A. M. Gillenwater, B. E. O'Neill, D. O. Lapotko, *Nat. Nanotechnol.* **2016**, *11*, 525–532.
- [63] J. Qi, H. Ou, Q. Liu, D. Ding, *Aggregate* **2021**, *2*, 95–113.
- [64] M. F. Kircher, A. de la Zerda, J. V. Jokerst, C. L. Zavaleta, P. J. Kempen, E. Mittra, K. Pitter, R. Huang, C. Campos, F. Habte, R. Sinclair, C. W. Brennan, I. K. Mellinshoff, E. C. Holland, S. S. Gambhir, *Nat. Med.* **2012**, *18*, 829–834.
- [65] C. Chen, X. Ni, H.-W. Tian, Q. Liu, D.-S. Guo, D. Ding, *Angew. Chem. Int. Ed.* **2020**, *59*, 10008–10012.
- [66] B. Yang, Y. Chen, J. Shi, *Angew. Chem. Int. Ed.* **2020**, *59*, 9693–9701.
- [67] W. Zhang, Y. Wen, D.-X. He, Y.-F. Wang, X.-L. Liu, C. Li, X.-J. Liang, *Biomaterials* **2019**, *193*, 12–21.
- [68] J. Qi, Y. Fang, R. T. K. Kwok, X. Zhang, X. Hu, J. W. Y. Lam, D. Ding, B. Z. Tang, *ACS Nano* **2017**, *11*, 7177–7188.
- [69] P. Wang, Y. Fan, L. Lu, L. Liu, L. Fan, M. Zhao, Y. Xie, C. Xu, F. Zhang, *Nat. Commun.* **2018**, *9*, 2898.
- [70] A. L. Vahrmeijer, M. Hutteman, J. R. van der Vorst, C. J. H. van de Velde, J. V. Frangioni, *Nat. Rev. Clin. Oncol.* **2013**, *10*, 507–518.
- [71] C. Wang, W. Fan, Z. Zhang, Y. Wen, L. Xiong, X. Chen, *Adv. Mater.* **2019**, *31*, 1904329.

RESEARCH ARTICLE

Entry for the Table of Contents

Insert graphic for Table of Contents here.



The compound with intense intramolecular motions exhibits amplified PA signal by specifically elevating the thermal-to-acoustic conversion efficiency, and the fluorescence brightness also increases due to the aggregation-induced emission signature. Based on the high-performance optical imaging agent, precise in vivo image-guided cancer surgery in different stages is conducted, greatly boosting the surgery outcome.